

# Context encoding enables machine learning based quantitative photoacoustics

Thomas Kirchner<sup>\*1,2</sup>, Janek Gröhl<sup>1,3</sup>, and Lena Maier-Hein<sup>\*1,3</sup>

<sup>1</sup>*Division of Computer Assisted Medical Interventions (CAMI), German Cancer Research Center (DKFZ), Heidelberg, Germany*

<sup>2</sup>*Faculty of Physics and Astronomy, Heidelberg University, Germany*

<sup>3</sup>*Medical Faculty, Heidelberg University, Germany*

June 12th, 2017

## Abstract

Real-time monitoring of functional tissue parameters, such as local blood oxygenation, based on optical imaging could provide groundbreaking advances in the diagnosis and interventional therapy of various diseases. While photoacoustic (PA) imaging is a novel modality with great potential to measure optical absorption deep inside tissue, quantification of the measurements remains a major challenge. In this paper, we introduce the first machine learning based approach to quantitative PA imaging (qPAI), which relies on learning the fluence in a voxel to deduce the corresponding optical absorption. The method encodes relevant information of the measured signal and the characteristics of the imaging system in voxel-based feature vectors, which allow the generation of thousands of training samples from a single simulated PA image. Comprehensive *in silico* experiments suggest that context encoding (CE)-qPAI enables highly accurate and robust quantification of the local fluence and thereby the optical absorption from PA images.

**Keywords:** photoacoustics, quantification, multispectral imaging, machine learning

## Introduction

Photoacoustic (PA) imaging is a novel imaging concept with a high potential for real-time monitoring of functional tissue parameters such as blood oxygenation deep inside tissue. It measures the acoustic waves arising from the stress-confined thermal response of optical absorption in tissue [1]. More specifically, a photoacoustic signal  $S(\mathbf{v})$  in a location  $\mathbf{v}$  is a pressure response to the locally absorbed energy  $H(\mathbf{v})$ , which, in turn, is a product of the absorption coefficient  $\mu_a(\mathbf{v})$ , the Grueneisen coefficient  $\Gamma(\mathbf{v})$  and the light fluence  $\phi(\mathbf{v})$ .

$$S(\mathbf{v}) \propto H(\mathbf{v}) = \mu_a(\mathbf{v}) \cdot \Gamma(\mathbf{v}) \cdot \phi(\mathbf{v}) \quad (1)$$

Given that the local light fluence not only depends on the imaging setup but is also highly dependent on the optical properties of the surrounding tissue, quantification of optical absorption based on the measured PA signal is a major challenge [2, 3]. So far, the field of quantitative PA imaging (qPAI) has focussed on model-based iterative optimization approaches to infer optical tissue parameters from measured signals (cf. e.g. [3–12]). While these methods are well-suited for tomographic devices with high image quality (cf. e.g. [13–15]) as used in small animal imaging, translational PA research with clinical

---

\*Please address all correspondence to t.kirchner@dkfz-heidelberg.de or l.maier-hein@dkfz-heidelberg.de

ultrasound transducers or similar handheld devices (cf. e.g. [1,16–22]) focusses on qualitative image analysis.

As an initial step towards clinical qPAI, we introduce a novel machine learning based approach to quantifying PA measurements. The approach features high robustness to noise while being computationally efficient. In contrast to all other approaches proposed to date, our method relies on learning the light fluence on a voxel level to deduce the corresponding optical absorption. Our core contribution is the development of a voxel-based *context image* (CI) that encodes relevant information of the measured signal voxel together with characteristics of the imaging system in a single feature vector. This enables us to tackle the challenge of fluence estimation as a machine learning problem that we can solve in a fast and robust manner. Comprehensive *in silico* experiments indicate high accuracy, speed, and robustness of the proposed context encoding (CE)-qPAI approach. This is demonstrated for estimation of (1) fluence and optical absorption from PA images, as well as (2) blood oxygen saturation as an example of functional imaging using multispectral PA images.

## Materials and Methods

A common challenge when applying machine learning methods to biomedical imaging problems is the lack of labeled training data. In the context of PAI, a major issue is the strong dependence of the signal on the surrounding tissue. This renders separation of voxels from their context - as in surface optical imaging [23] - impossible or highly inaccurate. Simulation of a sufficient number of training volumes covering a large range of tissue parameter variations, on the other hand, is computationally not feasible given the generally long runtime of Monte Carlo methods which are currently the gold standard for the simulation of light transportation in tissue [11].

Inspired by an approach to shape matching, where the shape context is encoded in a so-called *spin image* specifically for each node in a mesh [24], we encode the voxel-specific context in so-called context images (CIs). This allows us to train machine learning algorithms on a voxel level rather than image level and thus require orders of magnitude fewer simulated training volumes. CIs encode relevant information of the measured signal as well as characteristics of the imaging system (represented by so-called voxel-specific fluence contribution maps (FCMs)). The CIs serve as a feature vector for said machine learning algorithm which are trained to estimate fluence in a voxel. The entire quantification method is illustrated in Figure 1 which serves as an overview with details given in the following subsections.

### Fluence Contribution Map

An important prerequisite for computing the CI for a voxel  $\mathbf{v}$  is the computation of the corresponding FCM, referred to as  $\text{FCM}[\mathbf{v}]$ .  $\text{FCM}[\mathbf{v}](\mathbf{v}')$  represents a measure for the likelihood that a photon arriving in voxel  $\mathbf{v}$  has passed  $\mathbf{v}'$ . In other words, a FCM reflects the impact of a PA signal in  $\mathbf{v}'$  on the drop in fluence in voxel  $\mathbf{v}$ . An illustration of a FCM corresponding to a typical handheld PA setup is shown in Figure 1 (2). The  $\text{FCM}[\mathbf{v}]$  is dependent on how the PA excitation light pulse propagates through homogeneous tissue to arrive in  $\mathbf{v}$  given a chosen hardware setup. The  $x \times y$  FCMs per imaging plane are generated once for each new hardware setup and each voxel in the imaging plane.

In this first implementation of the CE-qPAI concept, FCMs are simulated with the same resolution as the input data assuming a background absorption coefficient of  $0.1 \text{ cm}^{-1}$  and a constant reduced scattering coefficient of  $15 \text{ cm}^{-1}$  [35]. The number of photons is varied to achieve a consistent photon count in the target voxel. The FCMs are generated with the widely used Monte Carlo simulation tool *mcxyz* [36]. We integrated *mcxyz* into the open-source Medical Image Interaction Toolkit MITK [37] as *mitkMcxyz* and modified it

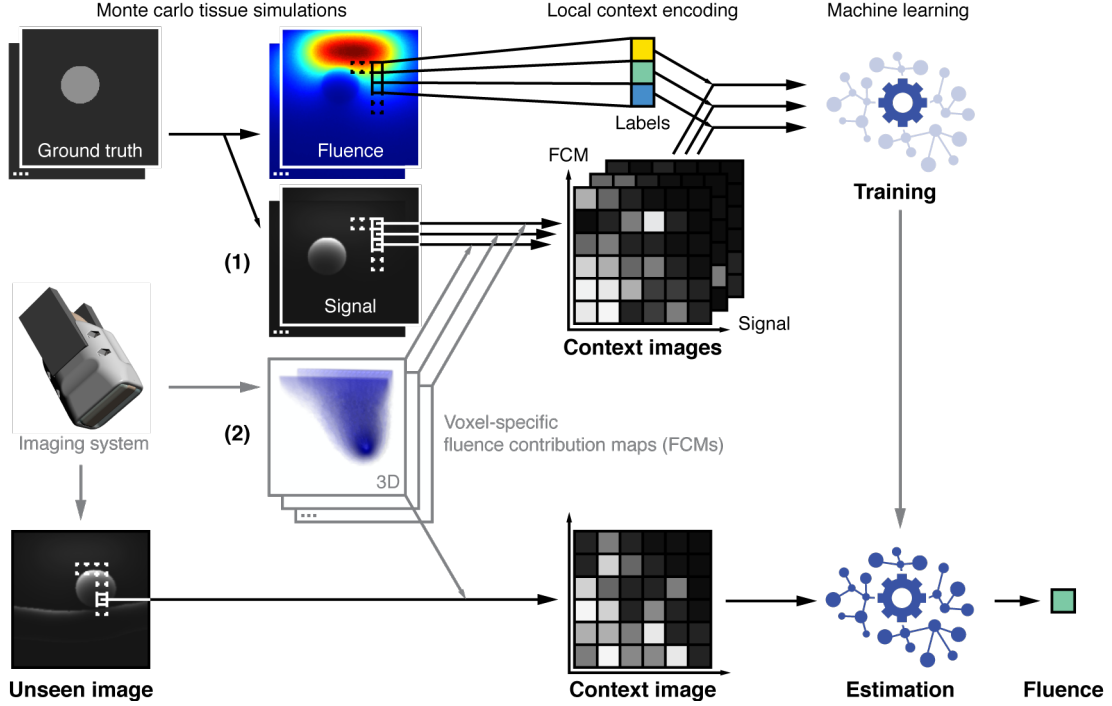


Figure 1: **Machine learning approach to fluence estimation with context images.** Context images (CIs) are generated individually for each voxel and encode both (1) relevant information on the measured signal extracted from the PAI signal volume and (2) prior knowledge on the characteristics of the imaging system represented by fluence contribution maps (FCMs). During algorithm training, a regressor is presented tuples of context images and corresponding ground truth fluence values for each voxel in the training data. For estimation of optical absorption in voxels of a previously unseen image, the voxel-specific context image is generated and used to infer the local fluence using the trained regressor.

to work in a multi-threaded environment. Sample FCMs for different voxels are illustrated in Figure 2, which also shows the generation of context images.

## Context Image

The CI for a voxel  $\mathbf{v}$  in a PA volume is essentially a 2D histogram composed of (1) the measured PA signal  $S$  in the tissue surrounding  $\mathbf{v}$  and (2) the corresponding  $\text{FCM}[\mathbf{v}]$ . More specifically, it is constructed from the tuples  $\{(S(\mathbf{v}'), \text{FCM}[\mathbf{v}](\mathbf{v}') | \mathbf{v}' \in N(\mathbf{v})\}$  where  $N(\mathbf{v})$  is defined as  $N(\mathbf{v}) = \{\mathbf{v}' | \text{FCM}[\mathbf{v}](\mathbf{v}') > \epsilon\}$ . This constraint is set to exclude voxels with a negligible contribution to the fluence in  $\mathbf{v}$ . The tuples are arranged by magnitude of  $S(\mathbf{v}')$  and  $\text{FCM}[\mathbf{v}](\mathbf{v}')$  into a 2D histogram and thereby encode the relevant context information in a compact form. In our prototype implementation of the CE-qPAI concept, the fluence contribution and signal axes of the histogram are discretized in 12 bins and scaled logarithmically to better represent the predominantly low signal and fluence contribution components. The ranges of the axes are set as  $0 < \log(S) < \log(255)$  and  $\log(\epsilon) < \log(\text{FCM}) < -1$ . Signals and fluence contributions larger than the upper boundary are included in the highest bin while smaller signals and fluence contributions are not. Figure 2 illustrates the generation of CIs from FCMs and PA signals. Labelled CIs are used for training a regressor that can later estimate fluence, which, in turn, is used to reconstruct absorption (Eq. 1).

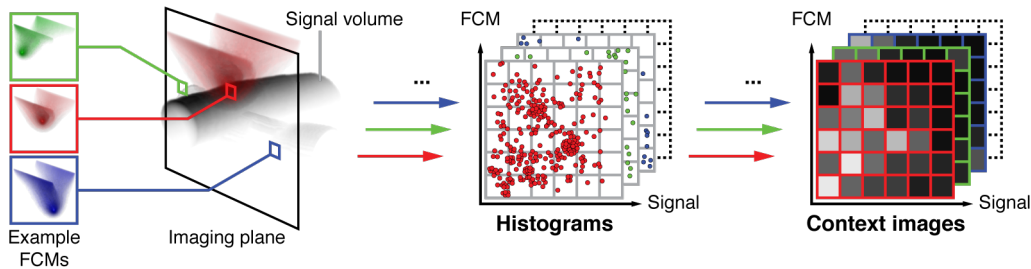


Figure 2: **Generation of context images** using FCMs and PA signal volumes. The voxel-specific FCMs serve as a representation of how the PA excitation light pulse propagates through homogeneous tissue to arrive in a target voxel given a chosen hardware setup. Signal volume and FCM are superimposed to generate 2D histograms from tuples of measured signal and corresponding fluence contribution.

## Machine learning based regression for fluence estimation

During the training phase, a regressor is presented tuples  $(CI(\mathbf{v}), \phi(\mathbf{v}))$  of context images  $CI(\mathbf{v})$  and corresponding ground truth fluence values  $\phi(\mathbf{v})$  for each voxel  $\mathbf{v}$  in a set of PAI volumes. For estimation of optical absorption in a voxel  $\mathbf{v}_u$  of a previously unseen image, the voxel-specific CI is generated and used to infer fluence  $\hat{\phi}(\mathbf{v}_u)$  using the trained algorithm.

In our prototype implementation of the CE-qPAI method we use a random forest regressor. With voxel-based CIs, thousands of training samples can be extracted from a single slice of a simulated PA training volume. Ground truth training data generation is performed using a dedicated software plugin integrated into MITK and simulating the fluence with `mitkMxyz`. It should be noted that the simulated images consist mainly of background voxels and not of vessel structures which are our regions of interest (ROI). This leads to an imbalance in the training set. To avoid poor estimation for underrepresented classes [38], we undersample background voxels in the training process to ensure a 1:1 ROI / background sample ratio. The parameters of the random forest are set to the defaults of `sklearn 0.18` using `python 2.7`, except for the tree count which was set to  $n_{\text{regressors}} = 100$ . CIs are used as feature vectors and labeled with the optical property to be estimated (e.g. fluence or oxygenation). The parameters were chosen based on a grid search on a separate dataset not used in the experiments of this work.

## Hardware setup

We assume a typical linear probe hardware setup [41] where the ultrasound detector array and the light source move together and the illumination geometry is the same for each image recorded. This is also the case for other typical tomographic devices [33, 34]. All simulation were performed on high-end CPUs (Intel i7-5960X).

## Experiments and Results

In the following validation experiments, we quantify the fluence up to an imaging depth of 28 mm in unseen test images for each dataset. With our implementation and setup, all images comprise 3008 training samples, which results in an average simulation time of 2 seconds per training sample. This allows us to generate enough training samples in a feasible amount of time, to train a regressor that enables fluence estimation in a previously unseen image in near real-time. The measured computational time for quantifying fluence in a single  $64 \times 47$  voxel image slice is  $0.9 \text{ s} \pm 0.1 \text{ s}$ .

In the following, we present the experimental design and results of the validation of CE-qPAI. First we will validate the estimation of absorption from PAI volumes acquired at

a fixed wavelength and then estimate blood oxygenation from multispectral PAI volumes.

## Monospectral absorption estimation

### Experiment

To assess the performance of CE-qPAI in PA images of blood vessels, we designed five experimental datasets with varying complexity as listed in Table 1. With the exception of  $\text{DS}_{\text{multi}}$ , each of the five experimental datasets is composed of 150 training items, 25 validation items and 25 test items, where each item comprises a 3D simulated PA image of dimensions  $64 \times 47 \times 62$  and 0.6 mm equal spacing as well as a corresponding (ground truth) fluence map.

Dataset	Vessel radius [mm]	Absorption coefficient $\mu_a$ [ $\text{cm}^{-1}$ ]	Vessel count
$\text{DS}_{\text{base}}$	3	4.7	1
$\text{DS}_{\text{radius}}$	<b>0.5 - 6</b>	4.7	1
$\text{DS}_{\text{absorb}}$	3	<b>1 - 12</b>	1
$\text{DS}_{\text{vessel}}$	3	4.7	<b>1 - 7</b>
$\text{DS}_{\text{multi}}$	0.5 - 6	1 - 12	1 - 7

Table 1: **Dataset design.** The design parameters of the datasets (DS)

As labels of the generated CIs we used a fluence correction  $\phi_c(\mathbf{v}') = \phi(\mathbf{v}')/\phi_h(\mathbf{v}')$ , where  $\phi_h(\mathbf{v}')$  is a fluence simulation based on a homogeneous background tissue assumption. We used 5 equidistant slices out of each volume, resulting in a generation of a total of 2,256,000; 376,000 and 376,000 context images for each dataset - for training, parameter optimization and testing respectively. To account for the high complexity of  $\text{DS}_{\text{multi}}$ , we increased the number of training volumes for that set from 150 to 400. The baseline dataset  $\text{DS}_{\text{base}}$  represents simulations of a transcutaneously scanned simplified model of a blood vessel of constant radius (3 mm) and constant absorption (vessel:  $4.73 \text{ cm}^{-1}$ , background:  $0.1 \text{ cm}^{-1}$ ) and reduced scattering coefficient ( $15 \text{ cm}^{-1}$ ). To approximate partial volume effects, the absorption coefficients in the ground truth images were Gaussian blurred with a sigma of 0.6 mm. Single slices were simulated using  $10^8$  photons and then compounded in a fully scanned volume. Different shapes and poses of the vessel were generated by a random walk defined with steps  $\mathbf{r}$  defined as

$$\mathbf{r}_i = \mathbf{r}_{i-1} + \eta \cdot \mathbf{a} \quad (2)$$

where  $\eta$  is a free parameter constant in each vessel with an inter-vessel variation within a uniform distribution ( $0 < \eta < 0.2$ ) and  $\mathbf{a}$  is varied for each of its components in each step within a uniform distribution ( $-0.2 \text{ mm} < a_i < 0.2 \text{ mm}$ ). To investigate how variations in geometry and optical properties impact the performance of our method, we designed further experimental datasets in which the number of vessels ( $\text{DS}_{\text{vessel}}$ ), the radii of the vessels ( $\text{DS}_{\text{radius}}$ ), the optical absorption coefficients within the vessels ( $\text{DS}_{\text{absorb}}$ ) as well as all of the above ( $\text{DS}_{\text{multi}}$ ) were varied. We tested the robustness of CE-qPAI to this range of scenarios without retuning CI or random forest parameters.

While most studies assess the performance of a method in the entire image (cf. e.g. [6, 26, 39]), it must be pointed out that the accuracy of signal quantification is often most relevant in a defined region of interest - such as in vessels or in regions which provide a meaningful PA signal. These are typically also the regions where quantification is particularly challenging due to the strongest signals originating from boundaries with discontinuous tissue properties. To address this important aspect we validated our method,

not only on the entire image, but also in the region of interest (ROI), which we define for our datasets as voxels representing a vessel and at the same time having a contrast to noise ratio (CNR) of larger than 2, to only include significant signal in the ROI. We define CNR following Walvaert and Rosseel [40] in a voxel  $\mathbf{v}$  as

$$\text{CNR} = \frac{S(\mathbf{v}) - \text{avg}(b)}{\text{std}(b)} \quad (3)$$

where the  $\text{avg}(b)$  and  $\text{std}(b)$  are the average and standard deviation of the background signal  $b$  over a simulated image slice with a background absorption coefficient of  $0.1 \text{ cm}^{-1}$  and no other structures. Using such an image without application of a noise model, we simulated an intrinsic background noise of  $(4.2 \pm 2.8)$  a.u.

To investigate the robustness of CE-qPAI to noise we added the following noise models to each dataset. The noise models consist of an additive Gaussian noise term applied on the signal volumes followed by a multiplicative white Gaussian noise term, similar to noise assumptions used in prior work [6, 26]. We examined three noise levels to compare against the simulation-intrinsic noise case:

- (1) 2% multiplicative and  $(0.125 \pm 0.125)$  a.u. additive component
- (2) 10% multiplicative and  $(0.625 \pm 0.625)$  a.u. additive component
- (3) 20% multiplicative and  $(1.25 \pm 1.25)$  a.u. additive component

The additive and multiplicative noise components follow an estimation of noise components on a custom PA system [41]. For each experimental dataset introduced in Table 1 and each noise set, we applied the following validation procedure separately. Following common research practice, we used the training data subset for training of the random forest and the validation data subset to ensure the convergence of the training process, as well as to set suitable parameters for the random forest and ROI, whereas we only evaluated the test data subset to report the final results (as described in [42]). As an error metric we report the *relative fluence estimation error*  $e_r$

$$e_r(\mathbf{v}) = \frac{|\hat{\phi}(\mathbf{v}) - \phi(\mathbf{v})|}{\phi(\mathbf{v})} \quad (4)$$

rather than an absorption estimation error, to separate the error in estimating fluence with CE-qPAI from errors introduced through simulation-intrinsic or added noise on the signal which will affect the quantification regardless of fluence estimation.

## Results

Figure 3 a-c show representative examples of the previously unseen 125 simulated test images from the baseline dataset  $\text{DS}_{\text{base}}$ , with their corresponding fluence estimation results. The optical absorption is reconstructed using the fluence estimation. A histogram illustrating absorption estimation accuracy in region of interest (ROI) voxels of  $\text{DS}_{\text{base}}$  is shown in Figure 3 d and compared with a static fluence correction approach.

Table 2 summarizes the descriptive statistics of the relative fluence estimation errors  $e_r$  for the experiments on absorption estimation using single wavelength PA images. The relative fluence estimation error  $e_r$  does not follow a normal distribution due to large outliers especially in complex datasets, which is why we report median  $e_r$  with interquartile ranges (IQR) for all datasets. Even for the most complex dataset  $\text{DS}_{\text{multi}}$  with variations of multiple parameters, specifically, number of vessels, vessel absorption coefficient and vessel radii CE-qPAI yields a median overall relative fluence estimation error  $e_r$  below 2%. Errors are higher in the ROI, especially in datasets with high variations of absorption.

Previously proposed qPAI approaches reveal high drops in estimation performance when dealing with noisy data (cf. e.g. [25]). To remedy this, methods have been proposed to

incorporate more accurate noise representations into model based reconstruction algorithms [26, 27]. When validating the robustness of CE-qPAI to noise, it yields high accuracy

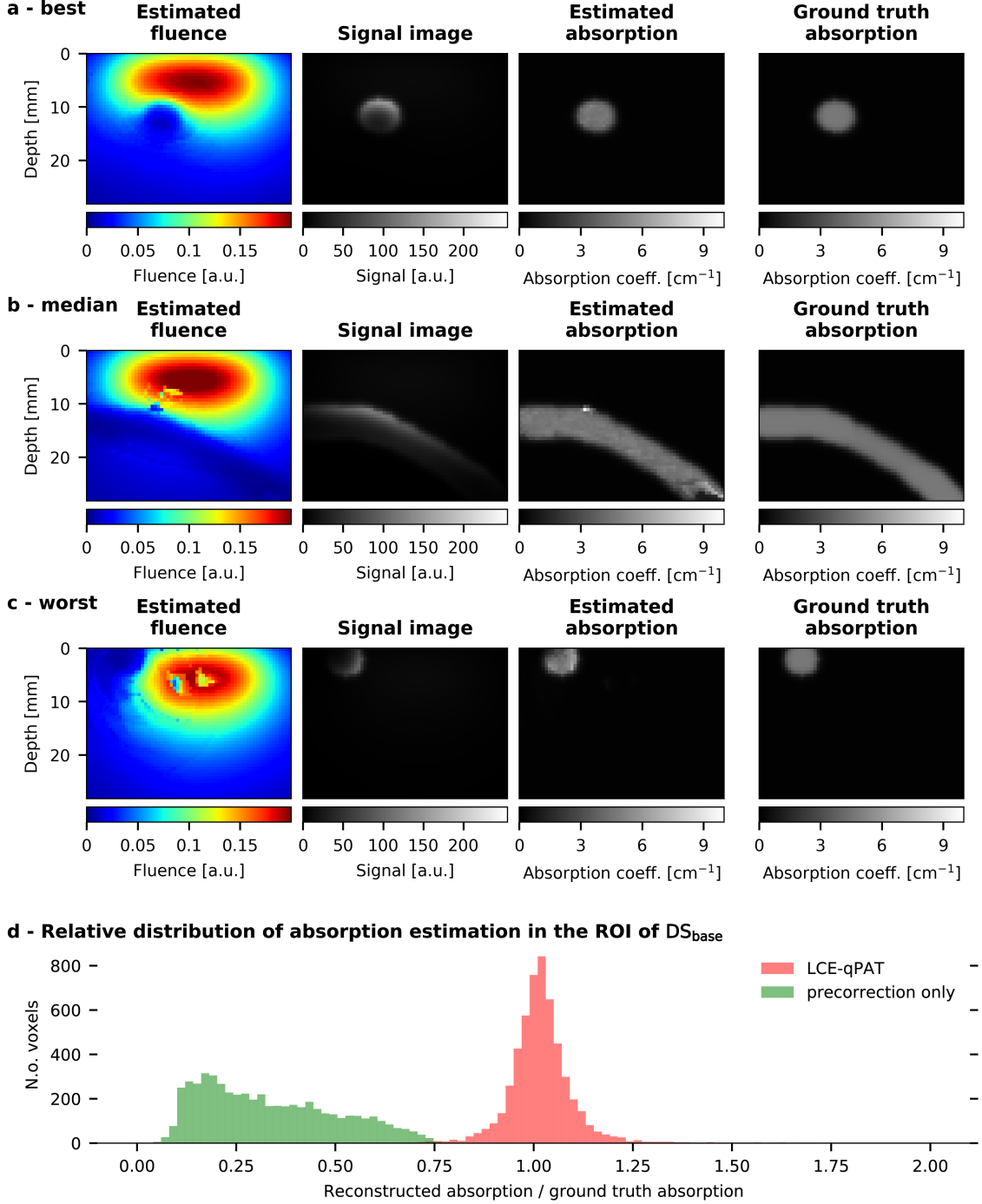


Figure 3: **Absorption reconstruction results after fluence estimation.** For the slices with the **a** lowest, **b** median, and **c** highest median fluence estimation error  $e_r$  within the region of interest (ROI) of  $\text{DS}_{\text{base}}$ . We show (from left to right) (1) the estimated fluence, (2) the corresponding signal images, (3) the resulting estimation of the absorption coefficient, and (4) the ground truth optical absorption, for reference. **d** shows a histogram of the relative absorption estimation over all ROI voxels ( $n = 5347$ ) in  $\text{DS}_{\text{base}}$  illustrating absorption estimation accuracy rather than fluence estimation accuracy measured by  $e_r$ . Precorrecting the signal with the fluence of a homogeneous tissue assumption underestimates the absorption and is considerably outperformed by CE-qPAI in the ROI. The CE-qPAI plot omits 5 outliers larger 2.

Dataset	Relative error $e_r$			
	All voxels		ROI	
	Median	IQR	Median	IQR
DS <sub>base</sub>	0.5 %	(0.2, 1.0) %	3.9 %	(1.9, 7.3) %
DS <sub>radius</sub>	0.8 %	(0.3, 2.7) %	5.8 %	(2.6, 11.4) %
DS <sub>absorb</sub>	0.7 %	(0.3, 1.9) %	14.0 %	(5.0, 31.5) %
DS <sub>vessel</sub>	1.6 %	(0.5, 5.9) %	6.8 %	(2.9, 13.4) %
DS <sub>multi</sub>	1.2 %	(0.4, 5.4) %	20.1 %	(7.3, 49.0) %

Table 2: **Descriptive statistics of fluence estimation results.** The median and interquartile range (IQR) of the relative fluence estimation error  $e_r$  for the five validation datasets used for the single wavelength experiments. The median error and IQR are provided (1) for all voxels in the respective test set as well as (2) for the voxels in the region of interest (ROI) only.

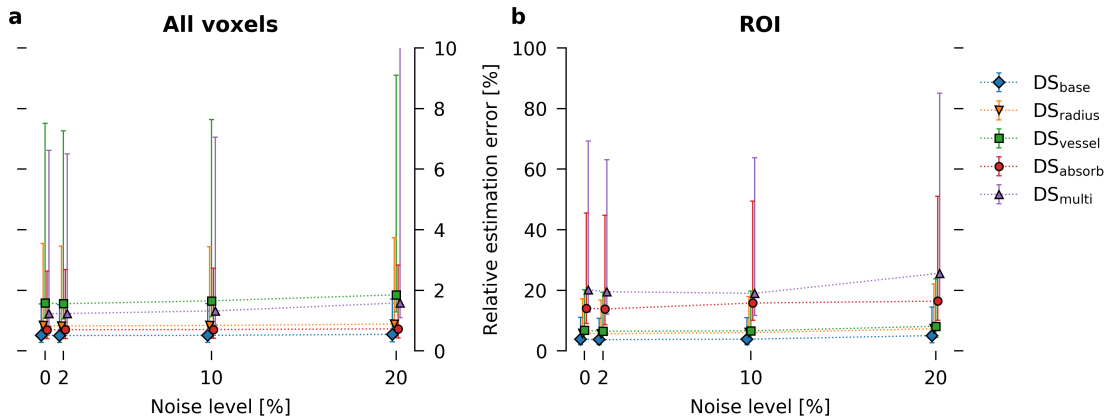


Figure 4: **Robustness of the fluence estimation against noise.** Median relative fluence estimation errors  $e_r$  with interquartile range over all datasets for, **a** all test voxels, and **b** in region of interest test voxels. The whiskers in this plot show the first and third quartile.

even under unrealistically high noise levels of up to 20% (cf. Figure 4). Regardless of the noise level applied, the highest median errors occur in the ROIs of datasets which are characterized by high absorption and inhomogeneous tissue properties.

## Multispectral blood oxygenation estimation

The concept of context encoding cannot only be used to estimate fluence and absorption but also derived functional parameters such as blood oxygenation. To this end, the estimated absorption in a voxel for multiple wavelengths can be applied to resolve oxygenation via linear spectral unmixing. Alternatively, a regressor can be trained using the CIs labeled with ground truth oxygenation.

## Experiment

To investigate the performance of CE-qPAI for blood oxygenation ( $sO_2$ ) estimation we designed an additional multispectral simulated dataset DS<sub>oxy</sub> using the wavelengths 750 nm, 800 nm and 850 nm. It consists of 240 multispectral training volumes and 11 multispectral test volumes, each featuring homogeneous oxygenation and one vessel with a radius of 2.3 to 4 mm - modeled after a carotid artery [43]. For each image slice and at each wavelength,  $10^7$  photons were used for simulation. Oxygenation values for the training

images were drawn randomly from a uniform  $sO_2$  distribution  $U(0\%, 100\%)$ . For testing, we simulated 11 multispectral volumes at 3 wavelengths and 11 blood oxygenation levels ( $sO_2 \in \{0\%, 10\%, 20\%, \dots, 100\%\}$ ). The optical absorption was adjusted by wavelength and oxygenation, as described by Jacques [35]. Hemoglobin concentration was assumed to be 150 g/liter [35]. The blood volume fraction was set to 0.5% in the background tissue and to 100% in the blood vessels. The reduced scattering coefficient was again set to  $15 \text{ cm}^{-1}$ . We estimated the oxygenation using three methods:

(1) *Linear spectral unmixing on the signal images as a baseline [28]*. For this, we applied a non-negative constrained least squares approach as also used in [15] that minimizes  $\|A\mathbf{x} - \mathbf{b}\| = 0$ , where  $A$  is the matrix containing the reference spectra,  $\mathbf{b}$  is the measurement vector, and  $\mathbf{x}$  is the unmixing result. Specifically, we used the python `scipy.optimize.minimize` function with the Sequential Least Squares Programming (SLSQP) method and added a non-negativity inequality constraint. We evaluated the unmixing results of this method on all voxels in the ROI as well as exclusively on those voxels with the maximum intensity projection (MIP) along image x-axis at wavelength 800 nm to account for nonlinear fluence effects deep inside the vessels.

(2) *Linear spectral unmixing of the signal after quantification of the three input images with CE-qPAI*. After correcting the raw signal images for nonlinear fluence effects using CE-qPAI, we applied the same method as described in (1) and evaluated on the same voxels that were used in (1) to ensure comparability of the results.

(3) *Direct estimation of oxygenation using a functional adaptation of CE-qPAI*. For functional CE-qPAI (fCE-qPAI), triples of CIs for the three chosen wavelengths were concatenated into one feature vector and labeled with the ground truth oxygenation.

## Results

Estimation of local blood oxygen saturation ( $sO_2$ ) is one of the main qPAI applications and is only possible with multispectral measurements. As such, the presented approaches were

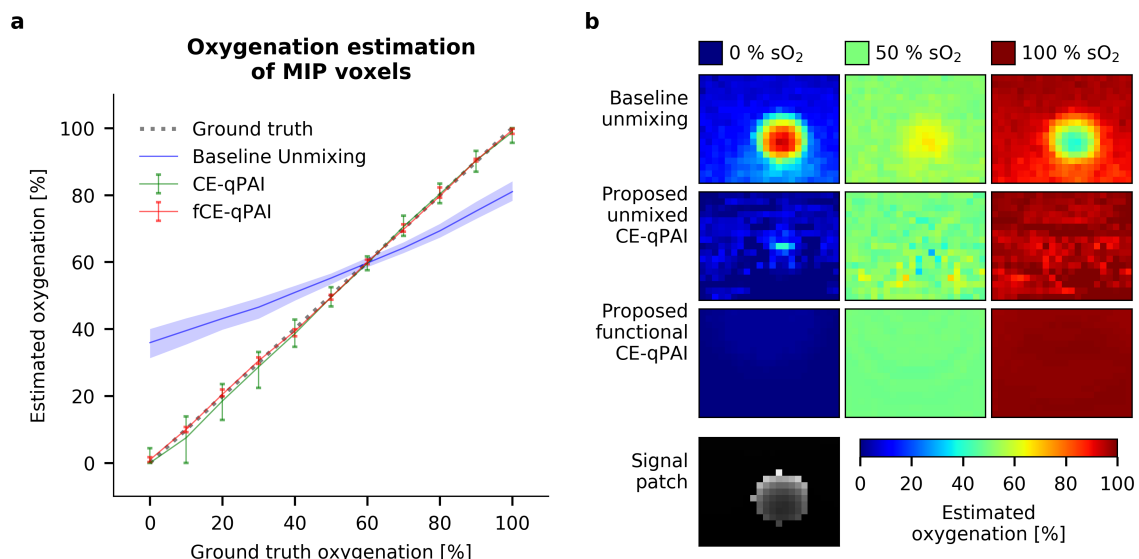


Figure 5: **Oxygenation estimation.** **a** shows the median oxygen estimation with the interquartile range (IQR) on the maximum intensity projection (MIP) voxels using linear spectral unmixing of (blue) the uncorrected signal, (green) the signal corrected by CE-qPAI, and (red) direct estimation by functional CE-qPAI (fCE-qPAI). **b** shows the oxygenation estimation for a representative patch of signal showing a vessel in 15 mm depth and with 3 mm radius. The signal for one of the measurement wavelengths is shown for reference together with the oxygen estimation results for 0%, 50%, and 100% ground truth homogeneous oxygenation and the three examined methods.

validated together with the baseline method on the dataset  $DS_{\text{oxy}}$ . As shown in Figure 5a, the estimation results for both methods are in very close agreement with the ground truth. In fact, the median absolute oxygen estimation error was 3.1 % with IQR (1.1 %, 6.4 %) for CE-qPAI and 0.8 % with IQR (0.3 %, 1.8 %) for the fCE-qPAI adaptation. Furthermore, our methodology outperforms a baseline approach based on linear spectral unmixing of the raw signal (as also compared to in [15]). By means of example Figure 5b shows that linear spectral unmixing of the ROI on the uncorrected signal fails deep inside the ROI where the fluence varies strongly for different wavelengths. To compensate for this effect when comparing the approach to our method, we validate all methods only on the maximum intensity projection along the depth axis (as also used in [29]) in Figure 5a.

## Discussion

This paper addresses one of the most important challenges related to photoacoustic imaging, namely the quantification of optical absorption based on the measured signal. In contrast to all other approaches proposed to qPAI to date (cf. e.g. [3–12]), our method relies on *learning* the light fluence in a voxel to deduce the corresponding optical absorption. Comprehensive *in silico* experiments presented in this manuscript show the high potential of this entirely novel approach to estimate optical absorption as well as derived functional properties, such as oxygenation, even in the presence of high noise.

Although machine learning methods have recently been applied to PAI related problems (cf. e.g. [44–46]), these have mainly focused on image reconstruction but not signal quantification. We attribute this to the fact that training generation for machine learning based qPAI is not at all straightforward given the lack of reference methods for estimating optical absorption in depth and the long simulation times of Monte Carlo based methods. Note also that commonly applied methods of data augmentation (i.e. methods that may be used to automatically enlarge training data sets as discussed in [47]) cannot be applied to PA images due to the interdependence of fluence and signal. There have been recent developments, however, that could speed up training data generation using hybrid diffusion approximation and Monte Carlo methods [48]. With our contribution, we have addressed the challenge by introducing the concept of context images, which allow us to generate one training case from each *voxel* rather than from each image.

As an important contribution with high potential impact, we adapted CE-qPAI to estimate functional tissue properties from multi wavelength data. Both variants - linear spectral unmixing of the fluence corrected signal, as well as direct estimation of oxygenation from multi wavelength CIs, yielded accurate results that outperformed a baseline approach based on linear spectral unmixing of the raw PA signal. It should be noted that linear spectral unmixing of the signal for  $sO_2$  estimation is usually performed on a wider range of wavelengths to increase accuracy. However, even this increase in number of wavelengths cannot fully account for nonlinear fluence effects [3]. Combined with the separately established robustness to noise, multi wavelength applications of CE-qPAI are very promising.

In our first prototype implementation of CE-qPAI we used random forests regressors with standard parameters. It should be noted, however, that fluence estimation from the proposed CI can in principle be performed by any other machine learning method in a straightforward manner. Given the recent breakthrough successes of convolutional neural networks [31], we expect even better performance of our approach when applying deep learning algorithms or using data augmentation in the training data generation process.

By relating the measured signals  $S(\mathbf{v}')$  in the neighborhood of  $\mathbf{v}$  to the corresponding fluence contributions  $FCM[\mathbf{v}](\mathbf{v}')$  we relate the absorbed energy in  $\mathbf{v}'$ , to the fluence contribution of  $\mathbf{v}'$  to  $\mathbf{v}$ . In this context it has to be noted that the fluence contribution  $FCM[\mathbf{v}](\mathbf{v}')$  is only an approximation of the true likelihood that a photon passing  $\mathbf{v}$  has previously passed  $\mathbf{v}'$ , because  $FCM[\mathbf{v}]$  is generated independently of the scene under

observation assuming constant background absorption and scattering. Nevertheless due to the generally low variance of scattering in tissue it serves as a reliable input for the proposed machine learning based quantification.

A limitation of our study can be seen in the fact that we performed the validation *in silico*. To apply CE-qPAI *in vivo*, further research will have to be conducted in two main areas. Firstly, the acoustical inverse problem for specific scanners must be integrated into the quantification algorithm to enable quantification of images acquired with common PAI probes such as clinical linear transducers. Secondly, training data has to be generated as close to reality as possible - considering for example imaging artifacts.

In contrast to prior work (cf. e.g. [6,7,26,32,39]) our initial validation handles the whole range of near infrared absorption in whole blood at physiological hemoglobin concentrations and demonstrates high robustness to noise. The impact of variations of scattering still needs investigation although these should be small in the near infrared.

Long-term goal of our work is the transfer of CE-qPAI to *clinical* data. In this context, run-time of the algorithm will play an important role. While our current implementation can estimate absorption on single slices within a second, this might not be sufficient for interventional clinical estimation of whole tissue volumes and at higher resolutions. An efficient GPU implementation of the time intensive CI generation should enable real-time quantification.

In summary, CE-qPAI is the first machine learning based approach to quantification of PA signals. The results of this work suggest that quantitative real-time functional PA imaging deep inside tissue is feasible.

## Disclosures

The authors have no relevant financial interests in this article and no potential conflicts of interest to disclose.

## Acknowledgements

The authors would like to acknowledge support from the European Union through the ERC starting grant COMBIOSCOPY under the New Horizon Framework Programme grant agreement ERC-2015-StG-37960.

We would like to thank the ITCF of the DKFZ for the provision of their computing cluster, C.Feldmann for her support with figure design. A.M.Franz, A.Seitel, F.Sattler, S.Wirkert and A.Vemuri for reading the manuscript.

## Author Contributions

T.K., J.G. and L.M. conceived of the research, analyzed the results and wrote the manuscript. T.K. and J.G. wrote the software and performed the experiments. L.M. supervised the project.

## Code and Data Availability

The code for the method as well as the experiments was written in C++ and python 2.7 and is partially open source and available at <https://phabricator.mtk.org/source/mitk.git>. Additional code and all raw and processed data generated in this work is available from the corresponding authors on reasonable request.

## References

- [1] Lihong V Wang and Junjie Yao. A practical guide to photoacoustic tomography in the life sciences. *Nat. Methods*, 13(8):627–638, 28 July 2016.
- [2] Lihong V Wang and Song Hu. Photoacoustic tomography: in vivo imaging from organelles to organs. *Science*, 335(6075):1458–1462, 23 March 2012.
- [3] B T Cox, J G Laufer, and P C Beard. The challenges for quantitative photoacoustic imaging. In *Photons Plus Ultrasound: Imaging and Sensing 2009*, 2009.
- [4] N Iftimia and H Jiang. Quantitative optical image reconstruction of turbid media by use of direct-current measurements. *Appl. Opt.*, 39(28):5256–5261, 1 October 2000.
- [5] B T Cox, S R Arridge, K P Kostli, and P C Beard. Quantitative photoacoustic imaging: fitting a model of light transport to the initial pressure distribution. In *Photons Plus Ultrasound: Imaging and Sensing 2005: The Sixth Conference on Biomedical Thermoacoustics, Optoacoustics, and Acousto-optics*, 2005.
- [6] Benjamin T Cox, Simon R Arridge, Kornel P Köstli, and Paul C Beard. Two-dimensional quantitative photoacoustic image reconstruction of absorption distributions in scattering media by use of a simple iterative method. *Appl. Opt.*, 45(8):1866–1875, 10 March 2006.
- [7] Zhen Yuan and Huabei Jiang. Quantitative photoacoustic tomography: Recovery of optical absorption coefficient maps of heterogeneous media. *Appl. Phys. Lett.*, 88(23):231101, 2006.
- [8] Jan Laufer, Dave Delpy, Clare Elwell, and Paul Beard. Quantitative spatially resolved measurement of tissue chromophore concentrations using photoacoustic spectroscopy: application to the measurement of blood oxygenation and haemoglobin concentration. *Phys. Med. Biol.*, 52(1):141–168, 7 January 2007.
- [9] Emma Malone, Ben Cox, and Simon Arridge. Multispectral reconstruction methods for quantitative photoacoustic tomography. In *Photons Plus Ultrasound: Imaging and Sensing 2016*, 2016.
- [10] Markus Haltmeier, Lukas Neumann, and Simon Rabanser. Single-stage reconstruction algorithm for quantitative photoacoustic tomography. *Inverse Probl.*, 31(6):065005, 2015.
- [11] Ben Cox, Jan G Laufer, Simon R Arridge, and Paul C Beard. Quantitative spectroscopic photoacoustic imaging: a review. *J. Biomed. Opt.*, 17(6):061202, June 2012.
- [12] Biswanath Banerjee, Srijeeta Bagchi, Ram Mohan Vasu, and Debasish Roy. Quantitative photoacoustic tomography from boundary pressure measurements: noniterative recovery of optical absorption coefficient from the reconstructed absorbed energy map. *J. Opt. Soc. Am. A Opt. Image Sci. Vis.*, 25(9):2347–2356, September 2008.
- [13] Lihong V Wang. Multiscale photoacoustic microscopy and computed tomography. *Nat. Photonics*, 3(9):503–509, 29 August 2009.
- [14] Jun Xia and Lihong V Wang. Small-animal whole-body photoacoustic tomography: a review. *IEEE Trans. Biomed. Eng.*, 61(5):1380–1389, May 2014.
- [15] Stratis Tzoumas, Antonio Nunes, Ivan Olefir, Stefan Stangl, Panagiotis Symvoulidis, Sarah Glasl, Christine Bayer, Gabriele Multhoff, and Vasilis Ntziachristos. Eigenspectra optoacoustic tomography achieves quantitative blood oxygenation imaging deep in tissues. *Nat. Commun.*, 7:12121, 30 June 2016.

- [16] Joël J Niederhauser, Michael Jaeger, Robert Lemor, Peter Weber, and Martin Frenz. Combined ultrasound and optoacoustic system for real-time high-contrast vascular imaging in vivo. *IEEE Trans. Med. Imaging*, 24(4):436–440, April 2005.
- [17] S Zackrisson, S M W Y van de Ven, and S S Gambhir. Light in and sound out: emerging translational strategies for photoacoustic imaging. *Cancer Res.*, 74(4):979–1004, 15 February 2014.
- [18] Paul Kumar Upputuri and Manojit Pramanik. Recent advances toward preclinical and clinical translation of photoacoustic tomography: a review. *J. Biomed. Opt.*, 22(4):41006, 1 April 2017.
- [19] John Gamelin, Andres Aguirre, Anastasios Maurudis, Fei Huang, Diego Castillo, Lihong V Wang, and Quing Zhu. Curved array photoacoustic tomographic system for small animal imaging. *J. Biomed. Opt.*, 13(2):024007, March 2008.
- [20] Kwang Hyun Song, Erich W Stein, Julie A Margenthaler, and Lihong V Wang. Noninvasive photoacoustic identification of sentinel lymph nodes containing methylene blue in vivo in a rat model. *J. Biomed. Opt.*, 13(5):054033, September 2008.
- [21] Chulhong Kim, Todd N Erpelding, Konstantin Maslov, Ladislav Jankovic, Walter J Akers, Liang Song, Samuel Achilefu, Julie A Margenthaler, Michael D Pashley, and Lihong V Wang. Handheld array-based photoacoustic probe for guiding needle biopsy of sentinel lymph nodes. *J. Biomed. Opt.*, 15(4):046010, July 2010.
- [22] Alejandro Garcia-Urbe, Todd N Erpelding, Arie Krumholz, Haixin Ke, Konstantin Maslov, Catherine Appleton, Julie A Margenthaler, and Lihong V Wang. Dual-Modality photoacoustic and ultrasound imaging system for noninvasive sentinel lymph node detection in patients with breast cancer. *Sci. Rep.*, 5:15748, 29 October 2015.
- [23] Sebastian J Wirkert, Hannes Kenngott, Benjamin Mayer, Patrick Mietkowski, Martin Wagner, Peter Sauer, Neil T Clancy, Daniel S Elson, and Lena Maier-Hein. Robust near real-time estimation of physiological parameters from megapixel multispectral images with inverse monte carlo and random forest regression. *Int. J. Comput. Assist. Radiol. Surg.*, 11(6):909–917, June 2016.
- [24] A E Johnson and M Hebert. Using spin images for efficient object recognition in cluttered 3D scenes. *IEEE Trans. Pattern Anal. Mach. Intell.*, 21(5):433–449, 1999.
- [25] Elena Beretta, Monika Muszkieta, Wolf Naetar, and Otmar Scherzer. 6. a variational method for quantitative photoacoustic tomography with piecewise constant coefficients. In *Variational Methods*. Walter de Gruyter, 2016.
- [26] Tanja Tarvainen, Aki Pulkkinen, Ben T Cox, Jari P Kaipio, and Simon R Arridge. Bayesian image reconstruction in quantitative photoacoustic tomography. *IEEE Trans. Med. Imaging*, 32(12):2287–2298, December 2013.
- [27] Tanja Tarvainen, Aki Pulkkinen, Ben T Cox, Jari P Kaipio, and Simon R Arridge. Image reconstruction with noise and error modelling in quantitative photoacoustic tomography. In *Photons Plus Ultrasound: Imaging and Sensing 2016*, 2016.
- [28] N Keshava and J F Mustard. Spectral unmixing. *IEEE Signal Process. Mag.*, 19(1):44–57, 2002.
- [29] Xosé Luís Deán-Ben, Erwin Bay, and Daniel Razansky. Functional optoacoustic imaging of moving objects using microsecond-delay acquisition of multispectral three-dimensional tomographic data. *Sci. Rep.*, 4:5878, 30 July 2014.

- [30] Keerthi S Valluru, Katheryne E Wilson, and Jürgen K Willmann. Photoacoustic imaging in oncology: Translational preclinical and early clinical experience. *Radiology*, 280(2):332–349, August 2016.
- [31] Kaiming He, Xiangyu Zhang, Shaoqing Ren, and Jian Sun. Deep residual learning for image recognition. In *2016 IEEE Conference on Computer Vision and Pattern Recognition (CVPR)*, 2016.
- [32] W Naetar and O Scherzer. Quantitative photoacoustic tomography with piecewise constant material parameters. *SIAM J. Imag. Sci.*, 7(3):1755–1774, 2014.
- [33] Volker Neuschmelting, Neal C Burton, Hannah Lockau, Alexander Urich, Stefan Harmsen, Vasilis Ntziachristos, and Moritz F Kircher. Performance of a multispectral optoacoustic tomography (MSOT) system equipped with 2D vs. 3D handheld probes for potential clinical translation. *Photoacoustics*, 4(1):1–10, March 2016.
- [34] Andrew Needles, Andrew Heinmiller, John Sun, Catherine Theodoropoulos, David Bates, Desmond Hirson, Melissa Yin, and F Stuart Foster. Development and initial application of a fully integrated photoacoustic micro-ultrasound system. *IEEE Trans. Ultrason. Ferroelectr. Freq. Control*, 60(5):888–897, May 2013.
- [35] Steven L Jacques. Optical properties of biological tissues: a review. *Phys. Med. Biol.*, 58(11):R37–61, 7 June 2013.
- [36] Steven L Jacques. Coupling 3D monte carlo light transport in optically heterogeneous tissues to photoacoustic signal generation. *Photoacoustics*, 2(4):137–142, 2014.
- [37] Ivo Wolf, Marcus Vetter, Ingmar Wegner, Marco Nolden, Thomas Bottger, Mark Hastenteufel, Max Schobinger, Tobias Kunert, and Hans-Peter Meinzer. The medical imaging interaction toolkit (MITK): a toolkit facilitating the creation of interactive software by extending VTK and ITK. In *Medical Imaging 2004: Visualization, Image-Guided Procedures, and Display*, 2004.
- [38] Andrew Estabrooks, Taeho Jo, and Nathalie Japkowicz. A multiple resampling method for learning from imbalanced data sets. *Comput. Intell.*, 20(1):18–36, 2004.
- [39] Roger J Zemp. Quantitative photoacoustic tomography with multiple optical sources. *Appl. Opt.*, 49(18):3566–3572, 20 June 2010.
- [40] Marijke Welvaert and Yves Rosseel. On the definition of signal-to-noise ratio and contrast-to-noise ratio for fMRI data. *PLoS One*, 8(11):e77089, 6 November 2013.
- [41] Thomas Kirchner, Esther Wild, Klaus H Maier-Hein, and Lena Maier-Hein. Freehand photoacoustic tomography for 3D angiography using local gradient information. In *Photons Plus Ultrasound: Imaging and Sensing 2016*, 2016.
- [42] Brian D Ripley. *Pattern Recognition and Neural Networks*. Cambridge University Press, 2007.
- [43] Jaroslaw Krejza, Michal Arkuszewski, Scott E Kasner, John Weigele, Andrzej Ustymowicz, Robert W Hurst, Brett L Cucchiara, and Steven R Messe. Carotid artery diameter in men and women and the relation to body and neck size. *Stroke*, 37(4):1103–1105, April 2006.
- [44] Austin Reiter and Muyinatu A. Lediju Bell. A machine learning approach to identifying point source locations in photoacoustic data. Proceedings Volume 10064, Photons Plus Ultrasound: Imaging and Sensing 2017;100643J (2017).

- [45] Andreas Hauptmann, Felix Lucka, Marta Betcke, Nam Huynh, Ben Cox, Paul Beard, Sebastien Ourselin and Simon Arridge. Model based learning for accelerated, limited-view 3D photoacoustic tomography. arXiv:1708.09832v1 [cs.CV].
- [46] Stephan Antholzer, Markus Haltmeier and Johannes Schwab. Deep Learning for Photoacoustic Tomography from Sparse Data. arXiv:1704.04587v2 [cs.CV].
- [47] Alexey Dosovitskiy, Jost T. Springenberg, Martin Riedmiller and Thomas Brox. Discriminative Unsupervised Feature Learning with Convolutional Neural Networks. *Advances in Neural Information Processing Systems*, 27, 766–774 2014.
- [48] Caigang Zhu and Quan Liu. Hybrid method for fast Monte Carlo simulation of diffuse reflectance from a multilayered tissue model with tumor-like heterogeneities. *J. Biomed. Opt.*, 17(1), 010501 2012.